Solar Physics
DOI: 10.1007/●●●●●-●●●-●●●-●●●●-●

A statistical study of 90–MeV proton events during the rising phase of solar cycle 23 observed with SOHO/ERNE

Firas Al-Hamadani[1] · Amjad Al-Sawad[2]

Abstract This study aims to comprehend solar and interplanetary (IP) phenomena generating solar energetic particle (SEP) events with proton energies exceeding 90MeV and identify the locations and commencement times of proton acceleration during such events. Forty energetic proton events, with intensities surpassing 10^{-3} cm^{-2} sr^{-1} MeV^{-1} at $\sim$ 94MeV, were meticulously selected from observations by the *Energetic and Relativistic Nuclei and Electrons* (ERNE) instrument onboard the *Solar and Heliospheric Observatory* (SOHO) during solar cycle 23. Using the fixed path length method (1.2AU) and velocity dispersion analysis (VDA), we estimated particle injection times, cross-validating results with the height of radio type II/IV burst emission and comparing them with flare and coronal mass ejection (CME) characteristics. All analyzed proton events were associated with CMEs, 27 with on-the-disk soft X-ray flares, and two void of any flare signatures. Radio type II/IV burst emission association was significant, and for non-associated events, one lacked radio emission while the other exhibited metric continuum and tilted type III burst lane emission. Protons were predominantly injected when CME leading edges were below 5R$_\odot$, reaching peak intensities above 10R$_\odot$ preceding the potential passage of IP shocks. In events where the CME front surpassed the estimated type II burst location, we propose a connection between type II bursts, CME interaction processes, and shocks at the CME flanks.

Keywords: Coronal mass ejections. Solar flares. Energetic particles, Protons, Propagation, Radio bursts, Meter-wavelengths and longer (m, dkm, hm, km), Type II

1. Introduction

The solar energetic particle events which have energy ranges from keV to GeV per nucleon, are particularly fascinating occurrences in solar physics that are frequently seen close to Earth. Their diverse sources, ranging from solar flares in the low corona to coronal shocks and IP shocks driven by CMEs, contribute to their complexity. Resolving the origin of SEP production involves a combination of observations and theoretical modeling, particularly addressing the

✉ F. Al-Hamadani
firas.balbool@uobasrah.edu.iq

A. Al-Sawad
dr.amjad@scrdiraq.gov.iq

[1] Department of Physics, University of Basrah, Basrah, Iraq

[2] Ministry of higher education and scientific research, Baghdad, Iraq

critical question: when does the acceleration initiate, relative to other manifestations of solar eruptions? Although the observational work on this issue is somewhat scattered. The CSHKP (Carmichael-Sturrock-Hirayama-Kopp-Pneuman) standard flare model is used by McCracken *et al.* (2023) to analyze the ground-level events (GLE) event that occurred on February 23, 1956, in detail using high time-resolution data. They improve our knowledge of how particles accelerate during solar flares and how it affects space weather occurrences later on. Cliver *et al.* (1982) proposed a delayed onset of high-energy ($>$ 500 MeV) protons by 15–20 minutes compared to Hα flares. Similar delays, corresponding to height differences for CMEs of 2–4$R_{\odot}$, have been reported in various studies, including those by (Kahler1994; Falcone *et al.*2003 ; Bieber *et al.*2004). For >90 MeV SEP events, understanding the events capable of producing such energetic protons and determining when and where the acceleration starts becomes crucial. Reames (2009a; 2009b), studied proton release times during GLE events and high-energy proton injections in solar flares. He calculated solar particle release times and deduced injection moments, revealing energetic protons release is linked to solar flare stages and CMEs.

Reames (1999) classified solar events into two classes based on soft X-ray signatures: 1) impulsive events, characterized by a high electron to proton (e/p) ratio, never associated with IP shocks, occurring low in the corona, and 2) gradual events, capable of accelerating particles to higher energies, well-associated with coronal and IP shocks, occurring high in the corona in extended regions. The two-class paradigm developed by Reames (1999) has been further explored, and various aspects of gradual and impulsive SEP events have been extensively compared and described by Reames (2013).

Impulsive SEP events typically manifest as low-intensity and short-duration occurrences, spanning hours to days. These events exhibit ion abundances with notable enhancements of ^{3}He and heavy ions in comparison to coronal abundances, and ion charge states that surpass typical coronal values. The maximum particle energies in impulsive events usually reach 10MeV per nucleon, and their observability is contingent upon the accompanying flare occurring in close proximity to the nominal root (at W60^{0}) of the IP magnetic field lines connected to the observer. It is widely accepted that particles in these events are primarily accelerated in impulsive solar flares Reames (1999). In contrast, gradual SEP events exhibit higher particle intensities, power-law energy spectra extending to higher energies (protons beyond 1 GeV in extreme cases), and prolonged durations ranging from days to weeks. They are well-correlated with CMEs and gradual soft x-ray flares. Interestingly, many gradual events also display composition signatures akin to impulsive events at energies >10 MeV/nucleon. Cane and Lario (2006), blurring the traditional distinction between impulsive and gradual events. They argue against a sharp division between the two SEP event classes, and the abundance variations no longer provide a clear separation. A comprehensive statistical analysis by Cane *et al.* (2010) of 280 solar proton events exceeding 25MeV concludes that the He/p ratio is not a reliable discriminator between classes, favoring a scenario where concurrent flare processes contribute particles in the majority of SEP events.

Long-duration events (LDEs) are a class of solar phenomena characterized by prolonged emission of X-rays and radio waves, often lasting several hours. These events are typically associated with large solar flares and the gradual release of energy resulting from magnetic reconnection processes in the solar corona (Kahler *et al.*, 1984). LDEs are of particular interest because they are often associated with the formation of CMEs (Harrison, 1995), which can contribute to the acceleration of high-energy SEPs. In addition, the long duration of these events and the complex energy release mechanisms make them a major focus in the study of solar dynamics and their effects on space weather (Cliver *et al.*, 1986). The role of IP shocks in accelerating energetic particles up to a hundred MeV has been acknowledged, with Klein and Trottet (2001) proposing that particles accelerated by solar flares may be trapped and further accelerated by CME-driven shocks, which are now recognized as a major contributor to SEP events acceleration.

Pohjolainen *et al.* (2016) presented a study highlighting the complexity of the acceleration and propagation mechanisms of SEPs and the importance of past solar activity in determining their properties. SEPs are primarily accelerated during the launch phase of CMEs, either via solar flares, coronal/IP shocks, or both. Studies such as (Rouillard *et al.* 2016; Afanasiev *et al.* 2018) have further explored SEPs acceleration at coronal and IP shocks, highlighting the role of high-energy SEPs and providing broader insights into SEPs acceleration mechanisms. Cliver 2016, suggest that the acceleration of high-energy protons in large SEPs events is more closely related to shock waves generated by CMEs rather than to solar flares, contradicting some recent hypotheses about the role of flares in these processes. Klein *et al.* 2022, present two scenarios: acceleration by a CME-driven shock; and acceleration within locked magnetic fields and subsequent release via magnetic reconnection. Both scenarios could be active in the same solar event, but to varying degrees. The data suggest that the first observed near-Earth relativistic particle release was associated with a type III emission, implying that magnetic reconnection played an important role in the release of the particles. In contrast, some other particles could have reached Earth through acceleration by the CME-related shock.

Understanding the timing of high-energy proton injection, whether associated with coronal or IP shocks or both, provides valuable insights into the location of the responsible eruption on heliocentric distances. Kahler 1994, analysis of >10 MeV proton onset times suggests that proton release near the Sun occurs not earlier than the maximum of the flare's impulsive phase. SOHO observations by Kocharov and Torsti (2002) emphasize that the potential of CMEs to produce accelerated particles in the IP medium critically depends on the development of solar eruptions below approximatly $2R_{\odot}$. Simnett 2002, analysis of energetic particle events from 1998 suggests that these events were unlikely to be accelerated in the IP medium by CMEs, but rather within the closed magnetic field regions of the corona. The complexity of the corona, as proposed by Sandroos and Vainio (2009), may provide the necessary conditions for particle acceleration. The characteristics of CMEs and their potential to produce accelerated particles in the IP medium are diverse. While CME transit speed is sometimes inversely correlated with proton production (Kahler, 2001), a general correlation between CME speed and SEP intensity is observed. However, no fast CMEs with widths less than 60^0 have been directly associated with SEPs event (Gopalswamy, 2003).

Recent studies further explore proton and electron acceleration at shocks, highlighting the role of shock parameters at connected field lines (Talebpour Sheshvan *et al.* 2023; Ameri *et al.* 2023; Dresing *et al.* 2022; Kouloumvakos *et al.* 2019). The association of radio emission with SEP events plays a crucial role in understanding eruption characteristics and acceleration mechanisms. Kahler (2001) notes that the occurrence of a type IV burst appears to be a common feature in most proton flares at energies >20 MeV. Later studies have shown a stronger association between SEPs event and type II radio bursts, as evidenced by Ameri, Valtonen, and Pohjolainen 2019. Type IV bursts, characterized by slowly drifting continuum emission, are usually attributed to trapped electrons in rising plasmoids (Leblanc *et al.*, 2001). Recent studies reveal that radio observations are essential for understanding the acceleration mechanisms and propagation dynamics of high-energy SEPs, providing valuable diagnostics for space weather research (Kolympiris *et al.* 2023; Kalaivani *et al.* 2020; Ameri, Valtonen, and Pohjolainen 2019; Kouloumvakos *et al.* 2015).

In contrast, type II radio bursts are believed to be produced by electrons accelerated at shock fronts. The relation between radio bursts and SEPs event remains a topic of great interest, with distinctions made between coronal type II bursts observed at decimetric-metric wavelengths and IP type II radio bursts at decametric-kilometric wavelengths. While IP type II bursts are often ascribed to shock waves driven ahead of a CME piston, the origins of coronal type II bursts are still debated. Associations between CMEs and type II bursts have been investigated, and the proximity of metric type II bursts with Decameter-Hectometer (DH) counterparts to SEPs is found to be more likely compared to metric type IIs without DH emission (Cliver *et al.* 2004; Gopalswamy *et al.* 2005). However, debates persist, with some studies suggesting both metric and DH type II bursts are driven by fast CMEs, while others propose a closer association between metric type II bursts and solar flares. Reiner *et al.* 2001, proposed a potential connection between the harmonic component of metric type IIs and DH type IIs. Additionally, Leblanc *et al.* 2001, put forth the argument that shock waves might be driven by CMEs throughout the entire distance from $1R_\odot$ to 1AU.

The timing of type III bursts has been proposed as crucial in distinguishing various types of proton events. Electron-rich, less intense SEPs event were found to exhibit type III bursts where electrons stream out along open magnetic field lines, marking their paths with plasma emission at the onset of flares, while the largest SEP events displayed type III bursts only after the flare's impulsive phase (Krucker *et al.*, 1999). Cane *et al.* 2002, had already highlighted that essentially all studied proton events are preceded by groups of type III bursts, suggesting that at least some interplanetary particles from well-connected flare regions can be anticipated. In a comprehensive study of 176 proton events with energy range 5580 MeV occurring from 1996 to 2016, Paassilta *et al.* 2017, employed the velocity dispersion analysis (VDA) method by Huttunen-Heikinmaa *et al.* 2005. which it is a technique used to determine the launch time of solar particles by analyzing their arrival times at different speeds. They examined 176 instances of SEPs from 1996 to 2016, and discovered that all of these occurrences were linked to CMEs and solar flares of at least C1.0 class. The importance of both CMEs and large solar flares in the acceleration and release of high-energy particles during SEP occurrences is highlighted by this thorough relationship.

This investigation specifically focuses on high-energy proton events producing an intensity of no less than 10^{-3} cm^{-2} sr^{-1} MeV^{-1} at energies of 90 MeV. The objective is to determine the heliocentric positions of the responsible eruptions, providing insights into mechanisms capable of injecting such protons. Characteristics of associated eruptions are deemed crucial, and the timing of all associated eruptions is thoroughly examined to elucidate potential relationships with the source of proton injection. Detailed information regarding the data analysis is provided in Section 2, observations are presented in Section 3, and Section 4 furnishes a summary with discussion. Finally, Section 5 encapsulates our conclusions.

2. Data Analysis

We utilize data from ERNE particle instrument onboar SOHO, comprising the Low Energy Detector (LED) and High Energy Detector (HED) (Torsti *et al.*, 1995). Proton identification relies on an on-board algorithm, yielding intensities in the energy ranges 1.314 MeV (LED) and 13140 MeV (HED) with one-minute time resolution.To determine proton event onset times, we employ up to 20 energy channels (ten LED and ten HED channels) using the method outlined by Huttunen-Heikinmaa *et al.* 2005. Assuming simultaneous release of particles with different energies near the Sun, the onset at 1 AU should be observed earlier at higher energies VDA is applied to fit release times and path lengths, a widely used analysis technique. Issues such as velocity dispersion turnover and differing detector sensitivities are considered in selecting energy channels for the VDA study, as outlined in Table 1. Also, the fixed path length method, using a common Archimedean spiral length of 1.2 AU, is employed for the same energies. This choice is in line with previous studies (Reames, 2009b) and the value is derived from proton and electron path lengths obtained by Krucker and Lin 2000.

While the assumption of scatter-free propagation holds for the first particles' propagation length, subsequent particles experience scattering due to plasma turbulence in the corona and IP space. Although mean free paths for scattering range from 0.01 to 1 AU, deconvolving transport effects is beyond this study's scope. However, the upper limit for the injection maximum is deduced by considering the time of observed maximum at 1 AU, adjusted for particle travel time from the Sun to Earth on the VDA-fitted or fixed path length. Various proton event characteristics are determined, including maximum intensity, rise time, whole event duration, and the ^{4}He/p ratio. Impulsive-or-gradual classification considers ^{4}He/p ratio, X-ray duration, SEP event duration at energies 20 and 90 MeV, and associated metric radio emission, aligning with previous studies.

To standardize timings with optical, radio, and soft X-ray data, eight minutes are added to all timings at the Sun. CME liftoff times from the SOHO/LASCO catalog are compared with injection times to identify associated CMEs. The CME liftoff time is calculated as the time averaged from extrapolations using linear and quadratic fits to CME height-time values. Soft X-ray and Hα flare characteristics are sourced from the Solar *Geophysical Data listings* (NGDC), while CME characteristics are obtained from the LASCO CME Catalog. We then compare the SEP injection times to the CME height-times in the LASCO catalog (quadratic fit), to estimate the heliocentric location of the CME at the time of the first injected protons and at the maximum intensity. The error limits for the CME height at injection time are obtained from the error limits of the proton injection times and the error limits of the quadratic CME height fits. Note that tracking the CME height below $2R_\odot$ has its problems.

The C1 corona-graph has not been available after 1998, and thus we depend on fitting the height-times of the CME using the C2 and C3 fields of view. In case of missing observations below $2R_\odot$ we calculate the approximate value for the height-time of the CME. Then, we estimate the heights of radio burst sources at proton injection times. For this, we use the hybrid atmospheric density model developed by Vršnak, Magdalenič, and Zlobec (2004), to convert plasma emission at the observed frequency to height at a corresponding density. As radio type II bursts have varying bandwidths, the center frequency of the emission lane was used in the calculations. As the observed radio emission can be assumed to be slightly above the electron plasma frequency, using the lane center should give reasonably reliable results. Type II bursts may also show both fundamental and harmonic bands, which sometimes are band split, and in these cases the calculations were done using the center frequency of the fundamental band. The method, its uncertainties, and alternative methods are described in, (*e.g.*, Cane *et al.*, 2010).

The use of atmospheric density models is not a trivial task since the local densities can vary and models differ from each other. The hybrid model is a synthesis of high-density low-corona models and IP density models, and it provides reasonable height estimates for a wide frequency range. However, one must remember that density models describe the undisturbed atmosphere and densities can change due to propagating transients, for example. We define the error of the height determination as the difference between the heights given by the Vršnak, Magdalenič, and Zlobec (2004) hybrid and the basic one-fold (Saito *et al.*, 1970) density profiles. This difference is used for both lower and upper error limits. This difference is used for both lower and upper error limits, for more information .

Dynamic radio spectra at Deci-metric wavelengths were provided by HiRAS/ *Hiraiso Solar Observatory* in Japan (25–2500 MHz), IZMIRAN/*Solar Radio Laboratory in Russia* (25–270 MHz), Nancay Decameter Array/Paris Observatory in France (20–70 MHz), and by the *Radio Solar Telescope Network* (RSTN) operated by the US Air Force at four different sites (25–180 MHz). The *Wind*/WAVES (Bougeret *et al.*, 1995) experiment records radio emission at DH wavelengths, from 14 MHz down to 20 kHz. Most of these data are available on each observatory/experiment Web page. At last, we compare the projections of the true heights on the plane of sky (obtained for fixed and VDA methods) in Figure 3, with the true heights of the radio bursts, which might give the closest results of heights.

3. Observations

We selected 40 events from the solar cycle 23, between September 1997 and October 2003, where protons were accelerated to over 90 MeV energies and had a maximum intensity above 10^{-3} cm^{-2} sr^{-1} MeV^{-1} on the >90 MeV energy. In selecting these events, we avoided event overlap in order to get the most accurate determination for the onset time. The most important point was to avoid the effect of mixed events that could be related to possibly two or more CMEs, very close to each other at the onset time. In addition, we left out about eleven events when ERNE or LASCO had gaps in their observations. A list of the > 90 MeV events, with their obtained characteristics, is presented in Table 1. This table illustrates the temporal characteristics of energetic particle events using two methods for calculating the injection time near the Sun. The first is the fixed-path method (1.2 AU) and the second is VDA. The onset time specifies the instant at which the highest-energy particles arrive at the observation site. The upper limit of maximum intensity is the latest possible time for the peak intensity of energetic solar particles to reach the observation site. The upper limit of maximum intensity is calculated using both methods to determine the expected peak time of the event, taking into account the uncertainty in the exact injection time at the Sun.

For the SEP event classification (Table 2), we considered the ^{4}He/p ratio, the X-ray event duration, and the event duration at 20 and 90 MeV, as the main factors. Pure Gradual (PG) events were those with the ^{4}He/p ratio less than 10^{-2}, the X-ray duration longer than one hour, and the SEP event duration more than one day. An event with none of these properties was considered as a Pure Impulsive (PI) event. If two factors were gradual and one impulsive we considered the event as Mixed Gradual (MG). An event with two impulsive and one gradual factor was considered as Mixed Impulsive (MI) event. The statistical distribution of maximum intensity demonstrates the fact that fundamental differences in acceleration physics are reflected in the classification of these events, as this distribution reveals the basic mechanisms of acceleration and transport. There is a systematic variation in intensity characteristics between different categories of events, with gradual events being characterized by a significant and noticeable increase in intensity, as shown in the Figure1.

3.1. Times of first injection and maximum intensity

The source region heliographic longitudes and the heights of the CMEs at first injection time (average between the two methods) are shown in Figure 2, together with the number distribution of CME heights at first injection and at the time of maximum injection (upper limit), and the

Table 1. Timeliness parameters for solar energetic particle events summarized using VDA and fixed path length (1.2 AU) techniques. Differences between the two analysis methodologies are highlighted in the table, which displays onset times, injection times, path lengths, and maximum intensity times for several occurrences.

No	DD.MM.YY	OT [1] UT	IT^2_F UT	Path Length [3] AU	IT^4_{VDA} UT	Max T^5_F UT	Max T^6_{VDA} UT
1	24.09.97	03:53	03:37	1.08 ± 0.19	3:40 ±6	05:03	05:06
2	04.11.97	06:37	06:21	1.37 ± 0.09	6:17 ±2	08:42	08:39
3	02.05.98	14:04	13:50	0.77 ± 0.09	13:58± 3	16:13	16:22
4	06.05.98	08:27	08:13	0.59 ± 0.03	8:25 ± 2	08:17	08:30
5	09.05.98	04:33	04:17	2.02 ± 0.11	3:52 ± 6	08:33	08:48
6	16.06.98	19:32	19:07	1.85 ± 0.06	18:47 ± 5	00:33	00:21
7	24.04.99	14:16	13:47	2.01 ± 0.09	13:22 ± 7	15:32	15:17
8	09.05.99	18:36	18:13	1.18 ± 0.16	18:18 ± 6	18:35	18:36
9	27.05.99	11:09	10:55	1.23 ±0.08	10:53 ± 5	12:12	12:12
10	01.06.99	19:52	19:36	1.49 ± 0.1	19:26± 3	2:37	2:32
11	11.06.99	01:09	00:53	1.11 ± 0.09	0:53 ± 3	01:12	01:14
12	18.01.00	18:33	18:17	1.62 ± 0.28	17:58 ± 9	19:59	19:52
13	18.02.00	09:52	09:36	1.49 ± 0.04	9:31 ± 2	10:47	10:42
14	23.04.00	14:00	13:41	1.68 ± 0.37	13:22 ± 13	19:25	19:16
15	06.06.00	19:25	18:06	1.25 ± 0.11	17:58 ± 12	05:53	05:53
16	10.06.00	17:25	17:09	1.05 ± 0.06	17:11 ± 2	17:33	17:36
17	14.07.00	10:36	10:20	1.67 ± 0.13	10:09 ± 5	14:11	14:02
18	22.07.00	12:04	11:51	2.22 ± 0.05	11:29 ± 4	12:13	11:54
19	12.09.00	13:04	12:42	1.30 ± 0.08	12:40 ± 3	17:38	17:37
20	16.10.00	07:34	07:09	1.59 ± 0.12	6:57 ± 6	09:12	09:05
21	08.11.00	23:19	23:03	0.46 ± 0.027	23:17 ± 1	UN	UN
22	24.11.00	05:47	05:31	2.06 ± 0.18	05:16 ± 9	07:39	07:23
23	28.01.01	16:50	16:37	1.86 ± 0.2	16:24 ± 7	18:49	18:37
24	29.03.01	10:52	10:27	1.96 ± 0.43	10:12 ± 16	16:25	16:11
25	02.04.01	12:25	12:06	1.84 ± 0.26	12:00 ±9	13:06	12:54
26	12.04.01	10:55	10:39	2.59 ± 0.2	10:08 ± 6	16:34	16:15
27	18.04.01	02:49	02:36	1.39 ± 0.14	2:30 ± 5	04:20	04:17
28	20.05.01	06:45	06:29	2.32 ± 0.1	5:43 ± 7	08:00	07:41
29	15.06.01	16:08	15:49	1.06 ± 0.16	15:56 ± 6	16:39	16:42
30	19.06.01	04:00	03:44	1.50 ± 0.26	03:46 ± 9	06:44	06:39
31	24.09.01	11:15	10:56	1.97 ± 0.15	10:38 ± 5	16:45	16:31
32	19.10.01	01:57	01:44	2.20 ± 0.19	1:23 ±6	03:29	03:10
33	22.10.01	15:45	15:23	1.33 ± 0.18	15:22 ± 6	23:18	23:16
34	04.11.01	16:51	16:38	1.23 ± 0.09	16:33 ± 5	17:21	17:21
35	22.11.01	20:54	20:35	1.95 ± 0.12	20:21 ± 5	0:33	0:19
36	26.12.01	05:41	05:25	1.25 ± 0.06	5:28 ± 3	10:05	10:05
37	21.04.02	01:41	01:28	1.28 ± 0.12	1:20 ± 6	01:51	01:55
38	22.08.02	02:28	02:06	2.05 ± 0.09	1:45 ± 5	02:49	02:33
39	24.08.02	01:30	01:17	1.36 ± 0.09	1:11 ± 3	01:46	1:44
40	26.10.03	17:52	17:36	1.25 ± 0.15	17:35 ± 4	17:54	17:54

[1] Onset time according to the highest energy channel.
[2] Injection Time (IT) for fixed 1.2 AU pathlength, corrected for 8 minutes to make it comparable to electromagnetic emission.
[3] Path length obtained from the VDA analysis.
[4] IT for VDA method.
[5] Upper time limit for maximum intensity, fixed 1.2 AU pathlength method.
[6] Upper time limit for maximum intensity, VDA method.

Table 2. SEPs event parameters: peak intensities, rise times (fixed path and VDA methods), ^{4}He/p ratios, durations at 20/90 MeV, and physical classification. UN denotes uncertain measurements..

No	DD.MM.YY	Max I[1]	$\triangle t\ ^{2}_{F}$ hour	$\triangle t\ ^{3}_{VDA}$ hour	^{4}He/P[4]	ED[5] hour	Class[6]
1	24.09.97	1.60E-3	1.43	1.43	3.24E-02	70-32	MI
2	04.11.97	7.20E-2	2.35	2.37	2.00E-02	54-50	MI
3	02.05.98	6.29E-2	2.38	2.40	8.29E-03	93-90	MG
4	06.05.98	1.79E-1	0.07	0.08	8.26E-03	67-48	MG
5	09.05.98	2.41E-3	4.52	4.68	2.32E-02	90-30	MI
6	16.06.98	1.05E-3	5.43	5.57	7.34E-03	105-63	PG
7	24.04.99	1.18E-3	1.75	1.92	7.77E-03	154-52	MI
8	09.05.99	1.16E-3	0.37	0.30	5.47E-03	77-8	MI
9	27.05.99	3.31E-3	1.28	1.32	3.63E-03	129-94	MG
10	01.06.99	7.88E-3	7.02	7.10	7.55E-03	168-45	MG
11	11.06.99	2.57E-3	0.32	0.35	2.83E-03	40-27	MG
12	18.01.00	1.39E-3	1.70	1.90	3.59E-03	14-11	MI
13	18.02.00	4.25E-3	1.18	1.18	1.38E-03	79-24	MI
14	23.04.00	1.25E-3	5.37	5.90	1.62E-03	54-36	MI
15	06.06.00	1.40E-3	11.78	11.92	2.02E-03	81-37	MG
16	10.06.00	3.82E-2	0.40	0.42	3.86E-03	110-54	MG
17	14.07.00	1.30E-1	1.60	3.85	3.53E-02	144-24	MI
18	22.07.00	3.22E-3	0.35	0.42	1.53E-03	60-17	MG
19	12.09.00	3.74E-3	4.93	4.95	9.18E-03	160-137	PG
20	16.10.00	2.94E-37	2.05	2.13	1.68E-03	144-58	PG
21	08.11.00	UN	UN	UN	8.00E-02	UN-UN	MI
22	24.11.00	3.82E-3	2.13	2.12	7.97E-03	39-24	MG
23	28.01.01	6.82E-3	2.20	2.22	1.34E-01	103-46	MI
24	29.03.01	3.09E-3	5.97	5.98	1.35E-02	48-13	MI
25	02.04.01	2.04E-3	1.00	0.90	2.89E-02	12-6	MI
26	12.04.01	1.56E-2	5.92	6.12	1.32E-02	54-24	MG
27	18.04.01	7.29E-2	1.73	1.78	9.13E-03	93-46	MG
28	20.05.01	8.51E-3	1.52	1.97	1.84E-02	41-16	MI
29	15.06.01	8.27E-3	0.88	0.77	7.69E-03	58-7	MG
30	19.06.01	3.00E-3	3.00	2.88	1.14E-02	UN-5	PI
31	24.09.01	1.79E-2	5.82	5.88	1.56E-02	155-144	MG
32	19.10.01	1.39E-3	1.75	1.78	7.51E-03	65-24	MG
33	22.10.01	3.87E-3	7.92	7.90	1.25E-02	96-48	MG
34	04.11.01	1.03E-1	0.72	0.80	7.47E-01	199-28	MI
35	22.11.01	6.80E-3	3.97	3.97	8.31E-02	33-33	MI
36	26.12.01	1.03E-1	4.67	4.62	1.89E-06	65-32	PG
37	21.04.02	1.00E-1	0.38	0.52	6.38E-03	216-104	PG
38	822.08.02	7.37E-3	0.72	0.77	5.81E-03	44-43	MG
39	24.08.02	1.10E-3	0.48	0.55	5.92E-03	94-66	MG
40	26.10.03	1.38E-2	0.30	0.32	2.26E-02	41-24	MG

[1]Maximum intensity, in $cm^{-2}\ sr^{-1}\ MeV^{-1}$.
[2]Ascending time, fixed 1.2 AU pathlength method.
[3]Ascending time, VDA method.
[4] ^{4}He-to-proton ratio.
[5]Event duration for 20 and 90 MeV protons, respectively (separated with a hyphen). UN stands for uncertain.
[6] Classification of SEP events; PI (Pure Impulsive), MI (Mixed Impulsive), PG (Pure Gradual), MG (Mixed Gradual).

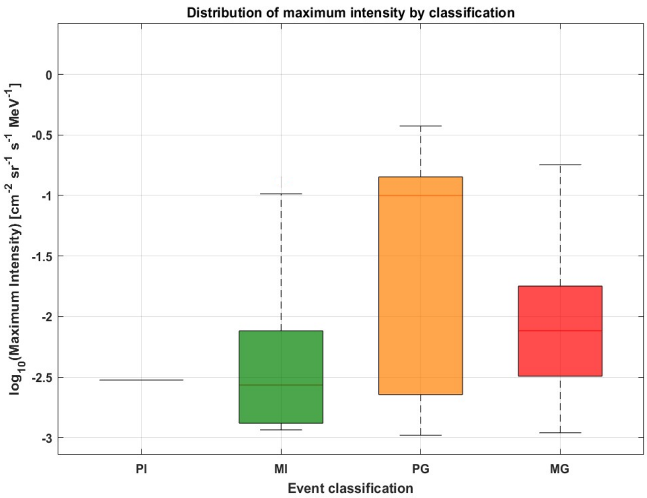

Figure 1. Statistical analysis of the intensity distribution of solar energtic particle events.

CME angular widths. For event 21, the time of maximum and the event duration at 90 MeV energy channel could not be determined, and thus it is not included in the event maximum statistics. As can be seen, most of the CMEs originated from active regions on the western hemisphere, and in eleven events the possible source region was estimated to be behind the western limb (longitude $>90^0$). In four events (events 17, 26, 35 and 40), VDA results in an unphysical CME height at injection time.

A physical height is, however, retained within the error limits in three of these events. Note that all four events give a physical value within the error limits for the fixed pathlength method. About 38% (15/39) of the CMEs were located beyond the field of view of LASCO C3 coronagraph ($30R_\odot$) at the time when the protons reached their maximum intensity. Only 13% (5/39) of the CMEs were located between (5–10)$R_\odot$ at the time of maximum intensity and 8% (3/39) were located below $5R_\odot$. At the $\sim$90 MeV energy channels the events have a short rise time and a long decay time, with less than one hour as a mean value for rising phase (i.e., difference in time between onset and maximum intensity, shown as Δt in Table 2, with a mean value of 0.88 hours) and 29 hours as a mean value for the whole duration of the events. However, in one exceptional case (the short-duration event 30) the rising phase of the event was found to be longer than the decay phase.

We found that most of the CMEs had heights between 1 and $5R_\odot$ at the time when protons were first injected, and the obtained CME heights are fairly similar with both SEP analysis methods. In eleven events the injection time was delayed in a sense that the CME had reached larger distances ($> 5R_\odot$) before the start of SEP injection, see Figure3. The figure also shows the calculated radio burst heights for comparison. The dashed line at $5R_\odot$ corresponds to a radio frequency of 4 MHz, calculated from the atmospheric density model. Examples of the analysed radio dynamic spectra are given in Figures. 4 and 5. These examples show the two different types, one with estimated injection time very early in the event (event 32, Figure 4) and one with a much later time (delayed event 15, Figure 5).

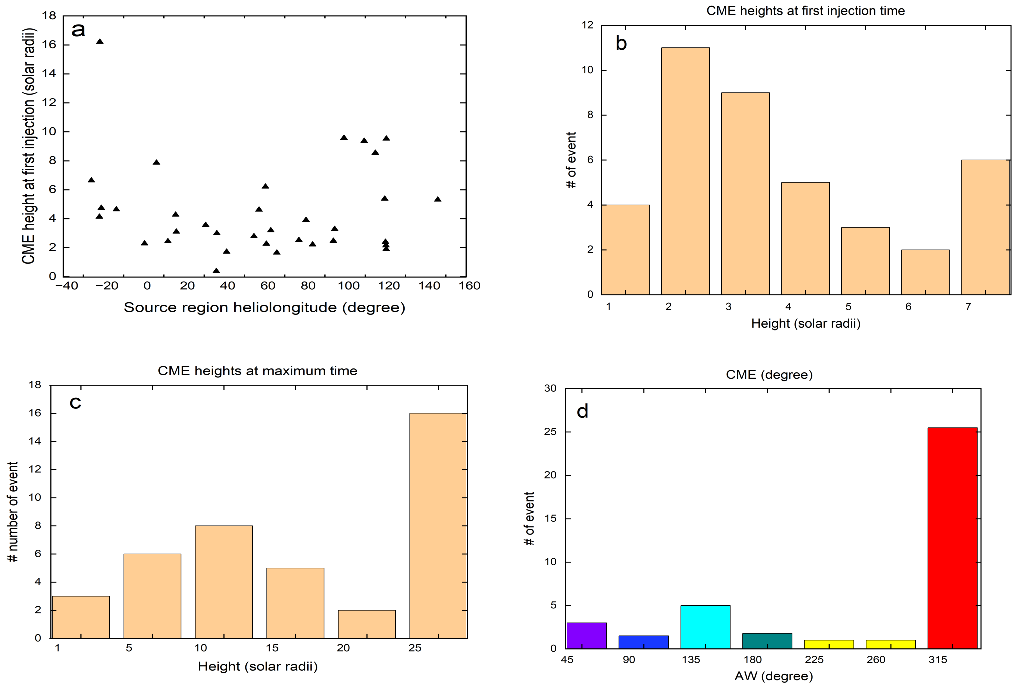

Figure 2. The CME heights (a) at first SEPs injection time (average from the two different methods of timing) vs. source region heliolongitude. Estimated longitude values are given also to behind-the-limb regions (longitude $>90^0$). Bar charts from (b to d) show the number distribution of CME heights at first injection time and at the time of maximum proton intensity, and the CME angular widths (AW).

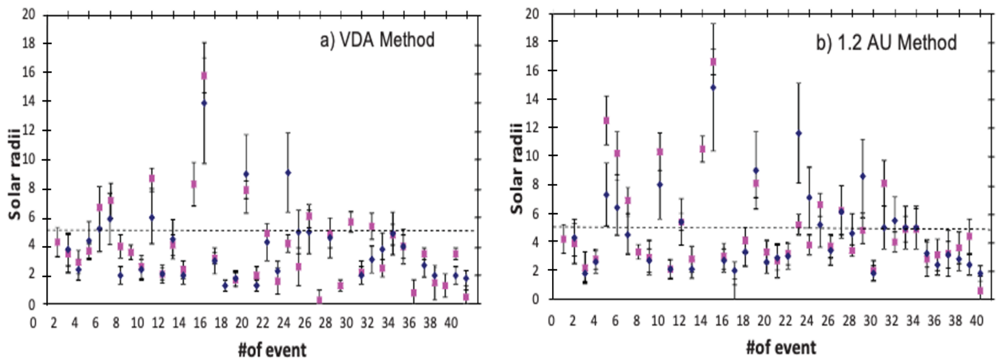

Figure 3. Estimated heights of CMEs (pink squares) and DH type II and IV bursts (blue diamonds) at the first proton injection time. The first injection time was determined with a) velocity dispersion analysis, b) 1.2 AU fixed path length method. The dashed line at $5R_\odot$ marks the separation between delayed events (where CME is located at heliocentric height $>5\ R_\odot$ at SEP injection time) and non-delayed events (CME height $<5\ R_\odot$ at SEP injection time).

3.2. Characteristics of associated eruptions

It may be expected that high-energy protons are mostly due to powerful eruptions. For the associated CMEs, this usually means high speed, wider angular width, western side, and a huge flux of SEPs. The >90 MeV proton events in this study were all associated with CMEs event. Of the CMEs, 65% (26/40) were halo CMEs. The CME angular widths were most typically between 315^0 and 360^0. For solar flares the most probable candidates for SEP sources are high-intensity, long duration X-ray flares. Of our SEP events, 82% (33/40) were associated with listed GOES soft X-ray flares. Of these flares 45% (15/33) were of GOES X-class, 48% (16/33) of M-class, and 6% (2/33) of C-class. The durations of the soft X-ray emission range from 5 minutes (event 27) to 151 minutes (event 20). Six of the 33 GOES flares were estimated to have the source region behind the western limb. Of the seven events that had no association with GOES flares, five were still estimated to have associated Hα activity behind the limb.

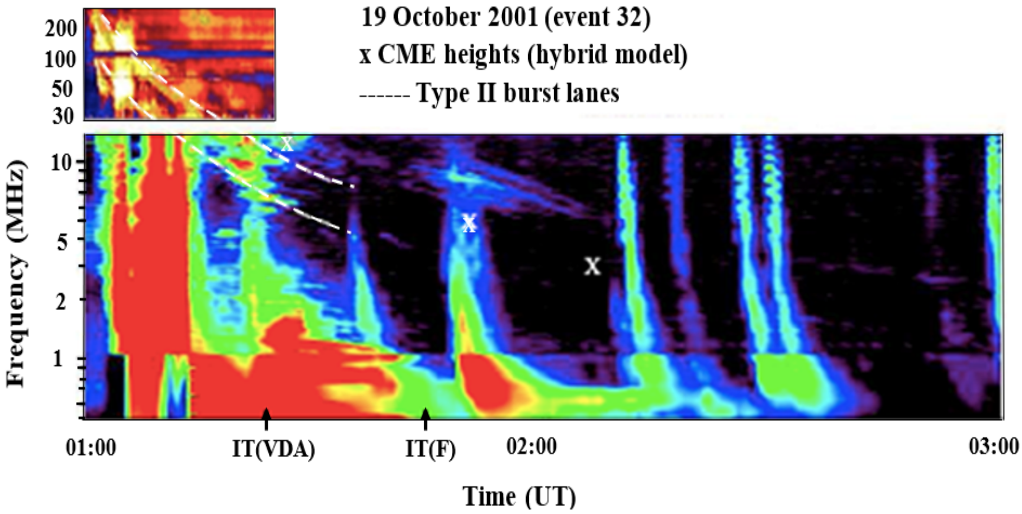

Figure 4. SEP event on 19 October 2001 (event 32). The spectral composite shows radio emission at 27025 MHz (HiRAS) and at 14 MHz– 500 kHz (Wind WAVES). The SEP injection times from the VDA method, IT(VDA) at 01:23 UT, and with the fixed path length method, IT(F) at 01:44 UT, are indicated in the plot. A metric type II burst with fundamental and second harmonic emission lanes (indicated with dashed lines) continues to DH wavelengths, but they cannot be followed below 4MHz, after 01:40 UT. The CME heights (frequencies corresponding to the LASCO CME leading edge height, calculated with the hybrid atmospheric density model) are marked with x.).

Only two events could not be connected to any observed or deduced flaring activity. Of the the eleven late injection events, more than half (6/11) were found to be associated with behind-the-limb activity, four events were associated with on-the-disk flaring, and one event was not connected to any observed flaring activity. The X-ray flares in our list were all associated with both metric and DH radio bursts. The CMEs associated with X-class solar flares had a mean speed of 1356 km s^{-1} and a mean width of 317^0, while the CMEs which were associated with M-class flares had a mean speed of 1209 km s^{-1} and a width of 273^0. The mean speed and angular width of all the CMEs was $\sim$1310 km s^{-1} and 289^0.

An association with metric type II, IV, and DH type II radio emission was found in 95% of the events (38/40). Specifically, 90% (36/40) of the events were associated with metric type II and/or IV bursts. 87% (35/40) of the events associated with DH type II radio emission .In 82% (33/40) of the cases, both metric type II/IV and DH type II emissions were present, with 42% (14/33) of these cases showing a continuous emission from metric to DH. Notably, only 15% (6/40) of the events showed no association with metric type II bursts. Among the type IV events, only 8% (2/24) lacked an associated type II burst, while 39% (14/36) of type II bursts did not have an associated type IV burst. Out of the 35 events with DH type II emissions, 11%

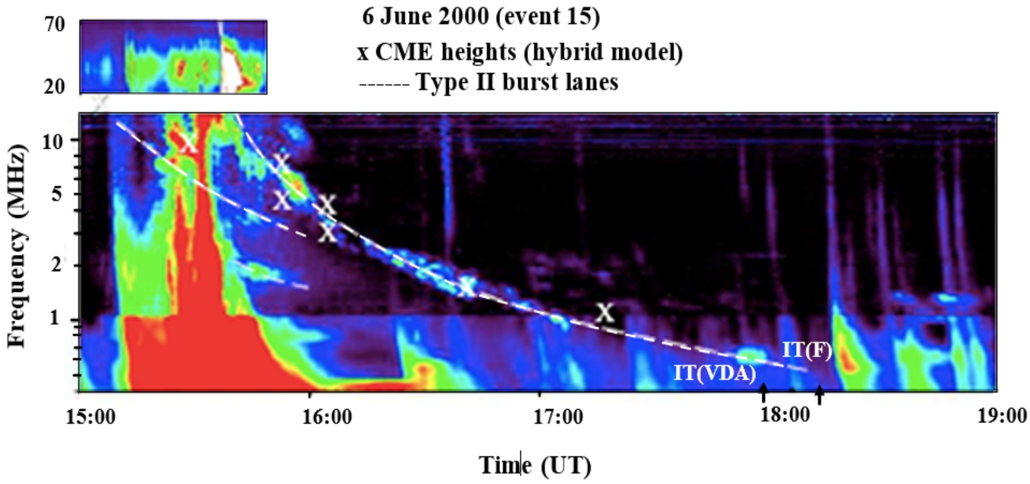

Figure 5. SEP event on 6 June 2000 (event 15). The spectral composite shows radio emission at 7020 MHz (Nancay Decameter Array) and at 14 MHz–400 kHz (Wind WAVES). The SEP injection times IT(VDA) at 17:58 UT and IT(F) at 18:06 UT are indicated in the plot. During this event at least three different CMEs were observed and the radio enhancements starting around 16:00 UT were probably due to CME interaction. Both SEP injection times took place after these radio signatures. CME heights and type II lanes are marked as in Figure 3.

(4/35) lacked associated metric type II and/or IV bursts. Of these, two events were associated with short-duration type IV-like emission, and one with decimetric emission. About 5% (2/35) were associated only with metric type IV emission, and 34% (12/35) were associated only with metric type II emission (see Table 3).

Interaction between CMEs may affect the SEP injection process as enhanced acceleration, but also as a delay due to the interfered magnetic connection between the lower (latter) CME and the IP space, since the field may open later in the interaction processes (Al-Sawad *et al.*, 2009). The events listed in Table 1, we find that events 1 and 30 are not in the CME interaction list of Gopalswamy *et al.* 2002, and that events 35–40 are not covered by their list. They classify our events 23 and 26 as major SEP events with no interaction, while event 14 is a minor SEP event with no interaction. Events 2, 4, 5, 7, 10, 13, 15, 16, 17, 18, 19, 20, 21, 22, 24, 25, 29, 31, and 33 are major SEP events with full interaction, (the preceding CMEs with intersecting trajectories have a position angle overlap 30^0 with the primary CMEs, whereas event 3 is a major SEP event with halo interaction (angle overlap $= 360^0$). Events 27 and 34 are major SEP events with streamer interaction, while event 32 is a major SEP event with partial interaction (angle overlap $\leq 30^0$). Events 6, 8, 11, 12, and 28 are minor SEP events with full interaction, and event 9 is a minor SEP event with streamer interaction. Thus, all our delayed events are listed as interaction events, with the exception of event 14.

4. Summary and Discussion

In this study, we have analyzed selected energetic 90 MeV proton events and the associated solar eruptions, and have obtained the CME and radio emission heights at the times of first SEP injections. Of the 40 SEP events themselves, 13% (5/40) were purely gradual, 45% (18/40) were mixed gradual, 40% (16/40) were mixed impulsive, and 2% (1/40) were purely impulsive.

Table 3. Characteristics of proton injections and radio emissions associated with CMEs. The table shows the CME heights measured by the fixed-path and VDA methods at the initial injection times and maximum injection periods, as well as the timings and spectral types of radio emissions.

	CME height at injection time				Solar flare characteristics		Radio emission	
Event No.	**h(IT_F)[1] $R_\odot$**	**h(IT_{VDA})[2] $R_\odot$**	**h(MIT_F)[3] $R_\odot$**	**h(MIT_{VDA})[4] $R_\odot$**	**GOES class (duration[5]) UT**	**Hα position**	**Type[6]**	**Start time[7] UT**
1	4.2 ± 1	4.3 ± 1	7.6 ± 1.5	7.7 ± 1.3	M5.9 (02:43–02:48-02:52)	S31E19	IV & II	02:48
2	3.9 ± 1.4	3.5 ± 1.3	14.8 ± 1.8	14.6 ± 1.7	X2.1 (05:52-05:58-06:02)	S14W33	II & IV	05:58 – 06:15
3	2.2 ± 1.1	2.9 ± 0.8	15.5 ± 1.1	16.1 ± 0.9	X1.1 (13:31-13:42-13:51)	S15W15	II & IV	13:38 – 13:42
4	2.8 ± 0.7	3.7 ± 0.5	3.2 ± 0.7	4.1 ± 0.4	X2.7 (07:58-08:09-08:20)	S11W65	IV & II	08:00 – 08:03
5	12.5 ± 1.7	6.7 ± 1.4	> 30	> 30	M7.7 (03:04-03:40-03:55)	SW100*	IV & II	03:23 – 03:26
6	10.2 ± 1.5	7.1 ± 1.2	> 30	> 30	M1.0 (18:03-18:42-19:28)	SW115*	II	18:18
7	6.9 ± 0.9	4.0 ± 0.8	18.4 ± 1	18.1 ± 0.9	—	SW150*	II	13:15
8	3.3 ± 0.5	3.6 ± 0.5	4.1 ± 0.5	4.6 ± 0.5	M7.6 (17:53-18:07-18:15)	NW95*	Cont	18:17
9	2.9 ± 1.2	2.6 ± 0.8	14.8 ± 1	14.8 ± 0.7	—	SW120*	II & IV	10:46 – 10:49
10	10.3 ± 1.3	8.7 ± 0.7	> 30	> 30	—	NW120*	Cont & II	18:47
11	2.1 ± 0.7	2.1 ± 0.4	3.6 ± 0.7	3.8 ± 0.4	—	NW120*	II & IV	00:39 – 00:51
12	5.4 ± 0.6	4.1 ± 0.7	12.2 ± 0.6	11.7 ± 0.7	M3.9 (17:07-17:27-17:44)	S19E11	II & IV	17:19 – 17:31
13	2.8 ± 0.9	2.4 ± 0.6	8.8 ± 0.9	8.4 ± 0.7	C1.1 (09:21-09:27-09:38)	S16W78	II	09:13
14	10.5 ± 0.9	8.3 ± 1.5	> 30	> 30	—	NW110*	—	—
15	16.6 ± 0.9	15.8 ± 1.2	> 30	> 30	X2.3 (14:58-15:25-15:40)	N20E18	IV & II	14:49 – 15:28
16	3.0 ± 0.9	3.2 ± 0.4	5.5 ± 0.9	5.8 ± 0.4	M5.2 (16:40-17:02-17:19)	N22W38	II	16:55
17	0.4 ± 1.4	2.3 ± 0.5	13.9 ± 1	12.7 ± 0.6	X5.7 (10:03-10:24-10:43)	N22W07	IV & II	10:08 – 10:17
18	4.1 ± 0.9	1.7 ± 0.5	6.6 ± 0.9	4.5 ± 0.5	M3.7 (11:17-11:34-12:02)	N14W56	IV & II	11:18 – 11:25
19	8.1 ± 1	7.9 ± 0.6	> 30	> 30	M1.0 (11:31-12:13-13:13)	S17W09	II	11:33
20	3.3 ± 0.8	2.0 ± 0.6	13.8 ± 0.9	13.0 ± 0.7	M2.5 (06:40-07:28-09:11)	NW95*	IV & II	06:47 – 06:54
21	2.7 ± 0.8	4.9 ± 0.2	UN	UN	M7.4 (22:42-23:28-00:05)	N20W66	IV	22:51
22	3.2 ± 0.8	1.6 ± 0.9	17.5 ± 0.9	15.7 ± 1	X2.0 (04:55-05:02-05:08)	N22W03	II	05:02
23	5.2 ± 0.7	4.2 ± 0.6	20.0 ± 0.7	20.3 ± 0.7	M1.5 (15:40-16:00-16:24)	S04W59	DCIM & II	15:22
24	3.8 ± 0.7	2.6 ± 1.3	> 30	28.0 ± 1.4	X1.7 (09:57-10:15-10:32)	N20W19	IV & II	09:58 – 10:03
25	6.6 ± 0.8	6.1 ± 0.8	11.7 ± 0.8	10.7 ± 0.8	X1.1(10:58-11:36-12:05)	N16W62	IV & II	11:05 – 11:19
26	3.7 ± 0.8	0.3 ± 0.7	> 30	> 30	X2.0 (09:39-10:28-10:49)	S19W43	II & IV	10:13 – 10:16
27	6.2 ± 1.7	4.9 ± 1	> 30	> 30	C2.2 (02:11-02:14-02:16)	SW120*	II	02:17
28	3.4 ± 0.4	1.3 ± 0.4	7.6 ± 0.4	6.7 ± 0.4	M6.4 (06:00-06:03-06:06)	SW120*	II	06:04
29	4.8 ± 0.9	5.7 ± 0.7	11.3 ± 1	11.7 ± 0.8	—	—	II	15:33
30	2.0 ± 0.7	2.2 ± 0.8	15.9 ± 0.7	15.5 ± 0.8	—	—	II	03:35
31	8.1 ± 1.6	5.4 ± 0.9	> 30	> 30	X2.6 (09:32-10:38-11:09)	S16E23	IV	09:24
32	4.0 ± 0.7	2.5 ± 0.6	15.5 ± 1.1	14.7 ± 1	X1.6 (00:47-01:05-01:13)	N16W18	IV & II	00:58 – 00:59
33	4.9 ± 0.9	4.8 ± 0.7	>30	> 30	M6.7 (14:27-15:08-15:31)	S21E18	IV & II	14:45 – 14:52
34	4.9 ± 1.4	4.0 ± 0.9	>30	> 30	X1.0 (16:03-16:20-16:57)	N06W18	II & IV	16:10 – 16:12
35	2.8 ± 1.2	0.8 ± 0.9	>30	> 30	M3.8 (20:18-20:36-20:52)	S25W67	II	20:22 – 20:27
36	3.1 ± 1.1	3.5 ± 0.4	>30	> 30	M7.1 (04:32-05:40-06:47)	N08W64	II & IV	04:59 – 05:20
37	3.2 ± 1.6	1.5 ± 1.2	>30	> 30	X1.5 (00:43-01:51-02:38)	S14W84	IV & II	01:17 – 01:018
38	3.6 ± 1.1	1.3 ± 0.8	21.2 ± 1.6	19.9 ± 1.5	M5.4 (01:47-01:57-02:05)	S07W62	II & IV	01:55 – 02:09
39	4.4 ± 1.2	3.5 ± 0.4	9.0 ± 1.2	8.7 ± 0.4	X3.1 (00:49-01:12-01:31)	S02W81	II & IV	01:01 – 01:15
40	0.6 ± 1	0.5 ± 0.5	> 30	> 30	X1.2 (17:21-18:19-19:21)	N02W38	II	17:35

[1] CME height at first injection time (fixed path length method).
[2] CME height at first injection time (VDA method).
[3] CME height at upper time limit of maximum injection (fixed path length method).
[4] CME height at upper time limit of maximum injection (VDA method).
[5] Duration listed as start time - time of maximum injection - end time. * From Cane et al. 2002.
[6] Listed spectral types are type II and type IV bursts, continuum emission (Cont), and decimetric emission (DCIM).
[7] Earliest and latest radio emission start times listed by the *Solar Geophysical Data Reports* (*National Geophysical Data Center*, NGDC).

We thus find that there is no indication that the ~90 MeV proton events could be purely gradual as they exhibit mostly mixed classification characteristics, indicating that the origin of the high-energy events is much more complex.

In most events analyzed, the CME was above the height of $2R_\odot$ at the time of the first particle injection, indicating that the acceleration of SEPs typically occurs when the CME is already well underway. However, notable exceptions were observed during the Bastille Day event and one of the Halloween events. For these events, both the VDA and the fixed path length methods yielded SEP injection times that occurred before the CME liftoff, suggesting that particles were injected into the IP medium even before the CME had fully erupted. The type II burst heights in these two events were also recorded below $2R_\odot$ at the times of injection, which indicates that low coronal shocks or the flare itself could have played a significant role in the early acceleration of particles that were observed at 1 AU. Furthermore, in eight other events, the VDA method produced CME heights of $\leq 2\ R_\odot$ at the time of SEP injection. However, in these cases, the fixed path length method indicated later injection times. This discrepancy between the two methods suggests that further analysis is needed to understand the exact timing and location of SEP acceleration in these events.

These observations are in line with those of Reames (2009a; 2009b), who also noted that acceleration of particles at lower coronal heights was frequently a part of GLE events, especially in the early phases of CME development. For several GLEs, Reames (2009a; 2009b) showed that the SEP onset dates could be tracked back to CME heights below $2R_\odot$. This supported the idea that early acceleration mechanisms, which may be associated with modest coronal shocks or flare activities, are important in these high-energy events. In most events (29/40), the CME was also below the height of $5R_\odot$ at the time of SEP maximum. While the eleven delayed events (injection at$>5\ R_\odot$) make up over 25% of all events, we have deduced explanations for the delays in all cases. Events 5, 6, 7, 10, 14, and 27 were connected to flares taking place behind the solar west limb. In such cases, it is natural to expect that the connection from the flare and CME liftoff site to the observing spacecraft is poor. In events 15, 19, and 31, the CMEs were clearly asymmetric, toward the northeast, south, and southeast, respectively, and again poor connection to the spacecraft can be expected. Finally, in events 25 and 27, the background from the previous SEP events may have influenced the SEP onset determination. Of the eleven delayed events, ten are also considered as possible interaction events, either with earlier CMEs or with a streamer.

The interaction between a CME and a streamer can significantly influence both the shock dynamics and the radio emissions associated with the event (see Al-Hamadani *et al.* 2017). Whene the Type II emission heights are much lower than the CME heights, it suggests that the radio emission source may be in the flank region of the CME where it interacts with a nearby streamer. As the CME shock wave passes through the streamer, it interacts with the magnetic structure of the plasma, enhancing the radio emission. This type of interaction may lead to sudden increases in frequencies or to the formation of broadband emissions in the radio spectrum. In the context of our findings, the two Reames (2009a; 2009b), papers and Gopalswamy *et al.* 2013, provide valuable insights into CME heights during SEP release in GLE events. Specifically, these studies highlight that CME heights at the SEP release time in GLE events tend to be relatively low, typically below $5R_\odot$, similar to the observations made in our study. As depicted in the top panel of Figure 2, our data shows that a significant number of CMEs were also below this height threshold at the time of the first SEP injection. This consistency suggests a broader pattern across different SEP events, reinforcing the notion that early CME dynamics play a crucial role in the acceleration and release of high-energy particles.

Interactions with other CMEs have been reported earlier by Gopalswamy *et al.* 2001, and the existence of an earlier CME can be considered to prevent access of the particles to the observing spacecraft. In the delayed events analyzed in this paper, it is difficult to separate the effects of poor connection due to the flare or CME liftoff location and the effects of interaction processes. However, signs of interaction were observed in the radio emissions in many of the events. All of the CMEs were estimated to be faster than 500 km s^{-1}, with the mean velocity of 1310 km s^{-1}. The mean CME width was 289^0. These findings are consistent with Gopalswamy *et al.* 2002,. Narrow CMEs ($< 60^0$) can indeed produce SEPs, but they are unlikely to generate the high-energy SEPs central to this study, we found one exceptional case (event 30) where the associated CME had an angular width of 58^0 and no Hα or soft X-ray counterparts.

The majority of the SEP events (38/40) were associated with metric and/or DH type II emission. The analyzed radio spectra show that only two of the events had DH type II emission without metric type IIs, but in both cases, other types of metric emissions were observed (continuum and decimetric bursts). Three events had metric emission but no DH bursts, and these were associated with CMEs with a mean width of 98^0, and a mean speed of 713 km s^{-1}. Only one halo CME was without any association with radio bursts, and the event was listed to include a behind-the-limb flare. Shanmugaraju *et al.* 2003, have earlier concluded that the CMEs with type IIs and type IVs are slightly wider and faster than the CMEs that have type IIs but no type IVs. We found that the CMEs associated with type II/IV bursts are wider than the CMEs with only type IIs, but they are not faster.

We also compared the heights of the type II bursts with the heights of the CME fronts at the times of SEP injection. As can be seen in Figure 2, there is no clear evidence supporting the idea that type II bursts are generated only at the leading fronts of the CMEs. In roughly half of the events, the CME front was above the type II burst location, a pattern observed particularly in the delayed injection events. This suggests that the radio type II emissions in these cases may be related to CME interaction processes and shocks at the CME flanks, rather than solely at the CME leading edge. This interpretation is consistent with previous studies, such as those by Zucca *et al.* 2018 and Jebaraj *et al.* 2021, which also highlight the possibility of type II bursts being associated with different parts of the CME or resulting from interactions with surrounding structures.

Our results are in agreement with the earlier findings Reames 2009a, where the first particles can reach energies of ∼90 MeV within a few tens of minutes after eruption, when the CME is still below $5R_\odot$. This relatively fast time scale for the acceleration sets strict requirements for the acceleration process. The most widely accepted mechanism for the acceleration of particles in these mostly gradual SEP events is the diffusive shock acceleration at CME-driven shock waves. Efficient particle acceleration in such shocks requires strong turbulence in the upstream region, while the rapid release of particles to interplanetary space requires low levels of turbulence further away from the shock. Kocharov *et al.* 1996 studied particle acceleration in a scenario where turbulence was strong in the low corona but weaker further out, due to the nonlinear evolution of the turbulence spectrum. However, it is often the turbulence generated by the particles themselves that is believed to enable fast and efficient acceleration of SEPs. The steady-state models for self-generated waves by Lee (1982) and Bell (1978) have now been extended into fully time-dependent directions by two groups, as discussed by Reames (2009b). These studies demonstrated that energies of ∼100 MeV can be achieved within 10 minutes of the initiation of acceleration, provided that the shock velocity and injection strength are sufficiently strong.

The self-generation of turbulence leads to trapping of particles near the shock, resulting in streaming-limited intensities during strong events. Consequently, particle intensities can peak at shock passage, reaching energies of ∼500 MeV in some cases (Reames, 2009a). In weaker events, Kahler (1994) suggested that maximum acceleration occurs when the shock is above 5 $R_\odot$ and the peak of the injection profile occurs when the associated CME reaches heights of 5–15 $R_\odot$. However, it's important to note that these results do not entirely exclude a potential flare contribution to particle acceleration, even if minor in some cases, as discussed by Kocharov *et al.* 2021 .

In this study, we have not conducted a full transport analysis and hence cannot give a precise moment of maximum acceleration. However, we can determine the upper limit for the maximum injection at 90 MeV, from the maximum of the observed intensity as described above. We find that for the majority of the events (24/39 for the VDA method, 23/39 for the fixed path length method), the CME was below 30 $R_\odot$ at the time of the maximum injection. For the remaining events, the CME is still far from 1 AU (e.g., for event 15, the CME is at a distance of 70 $R_\odot$) from the Sun at the time of the maximum intensity. Thus, in these events, the event maximum at 90 MeV is not caused by the passage of the shock of the spacecraft at 1 AU, but by earlier processes when the CME is at considerably lower heights.

The onsets of SEPs during GLE events were studied by Reames (2009a) using the velocity dispersion method. It was found that the SEP onset takes place after the type II onset, with the shock location estimated at 2–4 $R_\odot$ at the time of SEP onset. On the other hand, Aschwanden (2012) notes that half of the recent GLE events are accelerated during the impulsive flare phase, suggesting that in some events (e.g., Torsti *et al.* 1996; Torsti *et al.* 1999) a prompt SEP component is related to flare processes, while a delayed component may be related to extended flare acceleration or acceleration in CME-driven shock waves.

5. Conclusions

In our statistical study of the characteristics of the > 90 MeV proton events we found the following. All of the events were as sociated with CMEs and 82% of the CMEs were associated with visible on-the-disk solar flares. In 65% of the events the first protons were injected during the soft X-ray emission of solar flares. Of the flares, 45% were of GOES class X, 48% of class M, and 6

In 72% of the events the first protons were estimated to be injected while the leading edge of the CME was below $5R_\odot$. The delays in the eleven delayed events (i.e., where particle injection happened above the height of $5R_\odot$) were found to have been caused primarily by poor magnetic connections to the acceleration sites, or possibly in some cases due to interactions between CMEs and/or streamers. In two of the cases the background from a previous SEP event may have influenced the onset determination. The evaluation of the injection height measurements, by comparing the results from both methods (VDA and fixed path length of 1.2 AU) with the estimated type II burst heights, refined our calculations and two of the delayed events were considered as non-delayed after the re-evaluation.

In most events where the CME front was at height >5 $R_\odot$ at the time of first SEP injection, the radio type II emission was located at lower height, behind the CME front. These events were also found to be possible CME interaction events. This suggests plasma processes within the colliding/interacting CMEs, instead of relation to the CME bow shocks. It is also possible that the multiple transients had changed the atmospheric densities and therefore the height estimates for radio emission may contain larger errors, as they are no longer based on the standard non-disturbed densities of the solar corona.

In 79% of the events the CMEs were located above $10R_{\odot}$ when the proton events reached their maximum intensity. The average time for the rising phase to reach the maximum injection was about 0.88 hours, suggesting that acceleration to these energies takes place near the Sun. As most of the first protons were injected when the CME leading edges were below 5 $R_{\odot}$, and most of the protons reached their maximum injection while the CMEs were above 10 $R_{\odot}$, the maximum proton injection were reached much earlier than the CME-driven shocks would have passed the observing spacecraft. This suggests that the highest- energy particles were not accelerated efficiently by the CME driven shock near 1 AU. Our results confirm the idea that an earlier injection close to the Sun accompanies the liftoff of the CME and that SEP acceleration continues during different phases of the CME propagation near the Sun, decreasing in the interplanetary medium.

Declaration of Competing Interest

The authors declare that they have no known competing f inancial interests or personal relationships that could have appeared to influence the work reported in this paper.

Acknowledgments We extend our sincere appreciation to the ministry of higher education and scientific research of Iraq and university of Basrah, college of science, department of physics, for their invaluable support.We are grateful to all the individuals who have contributed by creating and updating the various solar event catalogues. The CME Catalog is generated and maintained at the CDAWData Center by NASA and the Catholic University of America in cooperation with the Naval Research Laboratory. The *Wind* WAVES radio type II burst catalogue has been prepared by Michael L. Kaiser and is maintained at the Goddard Space Flight Center. SOHO is a project of international cooperation between ESA and NASA.

References

Afanasiev, A., Vainio, R., Kocharov, L., Laitinen, T., Rouillard, A.P.: 2018, *Astron. Astrophys.* **614**, A4. DOI 10.1051/0004-6361/201731873

Al-Hamadani, F., Pohjolainen, S., Valtonen, E.: 2017, *Solar Phys.* **292**, 127. DOI 10.1007/s11207-017-1148-6

Al-Sawad, A., Saloniemi, O., Laitinen, T., Kocharov, L.: 2009, *Astron. Astrophys.* **497**, L1L5. DOI 10.1051/0004-6361/200912003

Ameri, D., Valtonen, E., Pohjolainen, S.: 2019, *Solar Phys.* **294**, 22. DOI 10.1007/s11207-019-1512-9

Ameri, D., Valtonen, E., Al-Sawad, A., Vainio, R.: 2023, *Adv. Space Res.* **71**, 2521. DOI 10.1016/j.asr.2022.12.014

Aschwanden, M.J.: 2012, *Space Sci. Rev.* **171**, 3. DOI 10.1007/s11214-011-9865-x

Bell, A.R.: 1978, *Mon. Not. Roy. Astron. Soc.* **182**, 147156. DOI 10.1093/mnras/182.2.147

Bieber, J.W., Evenson, P., Drge, W., Pyle, R., Ruffolo, D., Rujiwarodom, M., Tooprakai, P., Khumlumlert, T.: 2004, *Astrophys. J.* **601**, L103L107. DOI 10.1086/381801

Bougeret, J.-L., Kaiser, M.L., Kellogg, P.J., Manning, R., Goetz, K., Monson, S.J., Monge, N., Friel, L., Meetre, C.A., Perche, C., Sitruk, L., Hoang, S.: 1995, *Space Sci. Rev.* **71**, 231. DOI 10.1007/BF00751331

Cane, H. V., Erickson, W. C., Prestage, N. P.: 2002, *J. Geophys. Res.* **107**, A10, 1–15. DOI 10.1029/2001JA000320

Cane, H. V., Lario, D.: 2006, *Space Sci. Rev.* **123**, 45. DOI 10.1007/s11214-006-9011-3

Cane, H. V., Richardson, I. G., von Rosenvinge, T. T.: 2010, *J. Geophys. Res.* **115**, A08101. DOI 10.1029/2009JA014848

Cliver, E. W.: 2016, *Astrophys. J.* **832**, 128. DOI 10.3847/0004-637X/832/2/128

Cliver, E. W., Kahler, S. W., Shea, M. A., Smart, D. F.: 1982, *Astrophys. J.* **260**, 262. DOI 10.1086/160261

Cliver, E. W., Kahler, S. W., Reames, D. V.: 1986, *Astrophys. J.* **305**, 920–928. DOI 10.1086/164306

Cliver, E. W., Kahler, S. W., Reames, D. V.: 2004, *Astrophys. J.* **605**, 902–910. DOI 10.1086/382651

Falcone, A., Atkins, R., Benbow, W., et al.: 2003, *Astrophys. J.* **588**, 557–566. DOI 10.1086/373950

Dresing, N., Kouloumvakos, A., Vainio, R., Rouillard, A.: 2022, *Astrophys. J. Lett.* **925**, L21. DOI 10.3847/2041-8213/ac4ca7

Gopalswamy, N.: 2003, *Geophys. Res. Lett.* **30**, 12, 8013. DOI 10.1029/2003GL017277

Gopalswamy, N., Yashiro, S., Kaiser, M. L., Howard, R. A., Bougeret, J.-L.: 2001, *J. Geophys. Res.* **106**, A12, 29219–29230. DOI 10.1029/2001JA000234

Gopalswamy, N., Yashiro, S., Michalek, G., Kaiser, M. L., Howard, R. A., Reames, D. V., Leske, R., von Rosenvinge, T. T.: 2002, *Astrophys. J.* **572**, L103–L107. DOI 10.1086/341601

Gopalswamy, N., Aguilar-Rodriguez, E., Yashiro, S., Nunes, S., Kaiser, M. L., Howard, R. A.: 2005, *J. Geophys. Res.* **110**, A12. DOI 10.1029/2005JA011158

Gopalswamy, N., Xie, H., Akiyama, S., Yashiro, S., Usoskin, I. G., Davila, J. M.: 2013, *Astrophys. J. Lett.* **765**, L30. DOI 10.1088/2041-8205/765/2/L30

Harrison, R. A.: 1995, *Astron. Astrophys.* **304**, 585.

Huttunen-Heikinmaa, K., Valtonen, E., Laitinen, T.: 2005, *Astron. Astrophys.* **442**, 673–682. DOI 10.1051/0004-6361:20042620

Jebaraj, I. C., Kouloumvakos, A., Magdalenic, J., Rouillard, A. P., Mann, G., Krupar, V., Poedts, S.: 2021, *A&A* **654**, A64. DOI 10.1051/0004-6361/202141695

Kahler, S. W.: 1994, *Astrophys. J.* **428**, 837–843. DOI 10.1086/174292

Kahler, S. W.: 2001, *J. Geophys. Res.* **106**, 20947–20956. DOI 10.1029/2000JA002231

Kahler, S. W., Sheeley, N. R., Howard, R. A., Koomen, M. J., Michels, D. J.: 1984, *Sol. Phys.* **93**, 133–141. DOI 10.1007/BF00156658

Kalaivani, P. P., Shanmugaraju, A., Prakash, O., Kim, R. S.: 2020, *Earth Moon Planets* **123**, 61. DOI 10.1007/s11038-020-09533-9

Klein, K. L., Trottet, G.: 2001, *Space Sci. Rev.* **95**, 215–225. DOI 10.1023/A:1005236400689

Klein, K.L., Musset, S., Vilmer, N., Briand, C., Krucker, S., Battaglia, A. F., Dresing, N., Palmroos, C., Gary, D. E.: 2022, *Astron. Astrophys.* **663**, A173. DOI 10.1051/0004-6361/202243903

Kocharov, L., Torsti, J.: 2002, *Sol. Phys.* **207**, 149–157. DOI 10.1023/A:1015540311183

Kocharov, L. G., Torsti, J., Vainio, R., Kovaltsov, G. A.: 1996, *Sol. Phys.* **165**, 205. DOI 10.1007/BF00149100

Kocharov, L., Omodei, N., Mishev, A., Pesce-Rollins, M., Longo, F., Yu, S., Gary, D. E., Vainio, R., Usoskin, I.: 2021, *Astrophys. J.* **915**, 12. DOI 10.3847/1538-4357/abff57

Kolympiris, V., Papaioannou, A., Kouloumvakos, A., Daglis, I. A., Anastasiadis, A.: 2023, *Universe* **9**, 432. DOI 10.3390/universe9100432

Kouloumvakos, A., Nindos, A., Valtonen, E., Alissandrakis, C. E., Malandraki, O., Tsitsipis, P., Kontogeorgos, A., Moussas, X., Hillaris, A.: 2015, *Astron. Astrophys.* **580**, 17. DOI 10.1051/0004-6361/201424397

Kouloumvakos, A., Rouillard, A. P., Wu, Y., Vainio, R., Vourlidas, A., Plotnikov, I., Afanasiev, A., nel, H.: 2019, *Astrophys. J.* **876**, 80. DOI 10.3847/1538-4357/ab15d7

Krucker, S., Larson, D. E., Lin, R. P., Thompson, B. J.: 1999, *Astrophys. J.* **519**, 864–875. DOI 10.1086/307415

Krucker, S., Lin, R. P.: 2000, *Astrophys. J. Lett.* **542**, L61–L64. DOI 10.1086/312922

Leblanc, Y., Dulk, G. A., Vourlidas, A., Bougeret, J.-L.: 2001, *J. Geophys. Res.* **106**, 25301–25312. DOI 10.1029/2000JA000260

Lee, M. A.: 1982, *J. Geophys. Res.* **87**, 5063–5080. DOI 10.1029/JA087iA07p05063

McCracken, K. G., Shea, M. A., Smart, D. F.: 2023, *J. Space Weather Space Clim.* **72**, 3414–3427. DOI 10.1016/j.asr.2023.06.049

Paassilta, M., Raukunen, O., Vainio, R., Valtonen, E., Papaioannou, A., Siipola, R., Riihonen, E., Dierckxsens, M., Crosby, N., Malandraki, O., Heber, B., Klein, K.-L.: 2017, *J. Space Weather Space Clim.* **7**, A14. DOI 10.1051/swsc/2017013

Pohjolainen, S., Al-Hamadani, F., Valtonen, E.: 2016, *Sol. Phys.* **291**, 487–511. DOI 10.1007/s11207-015-0835-4

Reames, D. V.: 1999, *Space Sci. Rev.* **90**, 413–491. DOI 10.1023/A:1005105831781

Reames, D. V.: 2009a, *Astrophys. J.* **706**, 844–850. DOI 10.1088/0004-637X/706/1/844

Reames, D. V.: 2009b, *Astrophys. J.* **693**, 812–821. DOI 10.1088/0004-637X/693/1/812

Reames, D. V.: 2013, *Space Sci. Rev.* **175**, 53–92. DOI 10.1007/s11214-013-9958-9

Reiner, M. J., Kaiser, M. L., Gopalswamy, N., Aurass, H., Mann, G., Vourlidas, A., Maksimovic, M.: 2001, *J. Geophys. Res.* **106**, 25279–25290. DOI 10.1029/2000JA004024

Rouillard, A. P., Plotnikov, I., Pinto, R. F., Tirole, M., Lavarra, M., Zucca, P., Vainio, R., Tylka, A. J., Vourlidas, A., De Rosa, M. L., Linker, J., Warmuth, A., Mann, G., Cohen, C. M. S., Mewaldt, R. A.: 2016, *Astrophys. J.* **833**, 45. DOI 10.3847/1538-4357/833/1/45

Saito, K., Makita, M., Nishi, K., Hata, S.: 1970, *Ann. Tokyo Astron. Obs.* **12**, 53.

Sandroos, A., Vainio, R.: 2009, *Astron. Astrophys.* **507**, L21–L24. DOI 10.1051/0004-6361/200913228

Shanmugaraju, A., Moon, Y.-J., Dryer, M., Umapathy, S.: 2003, *Sol. Phys.* **217**, 301–317. DOI 10.1023/B:SOLA.0000006902.89339.e4

Simnett, G. M.: 2002, *Adv. Space Res.* **29**, 1493–1500. DOI 10.1016/S0273-1177(02)00213-2

Talebpour Sheshvan, N., Dresing, N., Vainio, R., Afanasiev, A., Morosan, D. E.: 2023, *Astron. Astrophys.***674**, A12. DOI 10.1051/0004-6361/202345908

Torsti, J., Valtonen, E., Lumme, M., Peltonen, P., Eronen, T., Louhola, M., Riihonen, E., Schultz, G., Teittinen, M., Ahola, K., Holmlund, C., Kelh, V., Leppl, K., Ruuska, P.: 1995, *Sol. Phys.* **166**, 505–531. DOI 10.1007/BF00733438

Torsti, J., Kocharov, L. G., Vainio, R., Anttila, A., Kovaltsov, G. A.: 1996, *Sol. Phys.* **166**, 135–158. DOI 10.1007/BF00179359

Torsti, J., Kocharov, L., Teittinen, M., Thompson, B. J.: 1999, *Astrophys. J.* **510**, 460–465. DOI 10.1086/306581

Vršnak, B., Magdalenič, J., Zlobec, P.: 2004, *Astron. Astrophys.* **413**, 753. DOI 10.1051/0004-6361:20034060

Zucca, P., Morosan, D. E., Rouillard, A. P., et al.: 2018, *Astron. Astrophys.* **615**, A89. DOI 10.1051/0004-6361/201732308